sustainability

MDPI

Article

Hydrochemical Characteristics and Genetic Mechanism of Geothermal Springs in the Aba Area, Western Sichuan Province, China

Minglu Sun [1,2,3], Xu Zhang [2,*], Xingcheng Yuan [3], Zhongyou Yu [2], Yao Xiao [2], Ying Wang [1,3] and Yunhui Zhang [3,4,*]

1 College of Engineering, Tibet University, Lhasa 850000, China
2 Chengdu Center of Hydrogeology & Engineering Geology, Sichuan Bureau of Geology & Mineral Exploration & Development, Chengdu 610081, China
3 Yibin Research Institute, Southwest Jiaotong University, Yibin 644000, China
4 State Key Laboratory of Geohazard Prevention and Geoenvironment Protection, Chengdu University of Technology, Chengdu 610059, China
* Correspondence: zhangxu1987613@163.com (X.Z.); zhangyunhui@swjtu.edu.cn (Y.Z.)

Abstract: Geothermal resources have been a source of significant clean energy in the world. The Sichuan Province is famous for its abundant geothermal resources in China, especially in western Sichuan. The Aba area is a significant minority region in northwestern Sichuan with abundant geothermal resources. In this study, hydrochemical and D-O analyses were conducted on the eight collected geothermal springs to investigate the genetic mechanism of the geothermal resource in the Aba area. The exposed temperatures and pH values of the geothermal springs ranged from 23 °C to 48 °C and from 6.6 to 9.5, respectively. Based on the hydrochemical characteristics, the eight geothermal springs were classified into two types: class A and class B. The class A geothermal springs belonged to the hydrochemical type of Ca-Mg-HCO_3-SO_4 and Ca-Mg-HCO_3 and were affected by the weathering and dissolution of carbonate and silicate. The class B hydrochemical type of geothermal spring was Na-HCO_3, which was determined by the weathering and dissolution of evaporite and silicate. A Na-K-Mg triangle diagram revealed that the geothermal springs belonged to immature water. A chalcedony geothermometer indicated that the temperature of the class A shallow geothermal reservoir in the Aba area was 59.70–73.00 °C and 70.65–120.91 °C for class B. Silicon enthalpy approaches showed that the initial reservoir temperature for class A was 181.36–203.07 °C (mixed by 85.76–89.44% cold water) and 271.74–295.58 °C (mixed by 87.39–87.54% cold water) for class B. The recharge elevation of the geothermal spring was 3415–3495 m as calculated by the D-O isotopes. We have proposed these genetic models of the two typical geothermal springs. The achievements provide a vital reference for the further development of geothermal water and the sustainable utilization of geothermal resources in the Aba area.

Keywords: hydrochemistry; D-O isotope; reservoir temperature; recharge source; genetic model; Aba area

Citation: Sun, M.; Zhang, X.; Yuan, X.; Yu, Z.; Xiao, Y.; Wang, Y.; Zhang, Y. Hydrochemical Characteristics and Genetic Mechanism of Geothermal Springs in the Aba Area, Western Sichuan Province, China. *Sustainability* **2022**, *14*, 12824. https://doi.org/10.3390/su141912824

Academic Editor: Rolf D. Vogt

Received: 13 September 2022
Accepted: 29 September 2022
Published: 8 October 2022

1. Introduction

Due to rapid economic growth and social development, environmental pollution and energy shortages are becoming serious issues around the world. Hence, it is urgent to find a renewable and clean energy, such as geothermal, wind, and solar energy. Among them, geothermal resources have been comprehensively utilized for heating, spas, and power generation worldwide [1–4]. So far, abundant geothermal resources have been reported in the western Sichuan Province, southwestern China [5–7]. To better exploit the geothermal resource, the understanding of the genetic mechanism should be improved in the western Sichuan Province.

The western Sichuan Province consists of the Garze and Aba area. Over the years, a lot of research work has been conducted on the geochemical characteristics, genetic mechanism, and regional geological background of the geothermal resources in the Garze area of the western Sichuan Province [8,9]. Tang et al. (2017) investigated the deep thermal structure beneath the western Sichuan Province [10]. Shi et al. (2017) provided a preliminary classification of the hyrochemical types of geothermal water in the western Sichuan Province [11]. Scholars analyzed the genetic mechanism of geothermal springs in the Xianshuihe, Ganzi–Litang, and Batang geothermal belts [8,12–14]. The Kangding geothermal field has been regarded as an area with a great potential for geothermal utilization in the western Sichuan Province [15]. Hence, significant attention has been paid to the Kangding geothermal field in recent years. In the Kangding field, the hydrochemical type of geothermal water found in the north is mainly of the$Na\text{-}HCO_3$ type; in the south, the geothermal water is mainly of the $Na\text{-}Cl\text{-}HCO_3$ type [16]. The hydrogeochemical processes, calcite scaling, and heat flux have been analyzed in the Kangding geothermal field, respectively. Geothermal springs have also been reported in the Aba area of northwestern Sichuan. However, there have been less studies on the hydrochemical characteristics and genetic mechanisms of the geothermal resources in the Aba area, which has hindered the efficient and reasonable utilization of these geothermal resources.

Therefore, this study aimed to elucidate the genetic mechanism of the geothermal springs in the Aba area. Eight geothermal spring samples were collected for hydrogeochemical and D-O isotope analyses. This study clarified the water–rock interactions, reservoir temperatures, and recharge sources of the geothermal water. Afterwards, a conceptual genetic model of geothermal springs was proposed. The achievements should provide a vital reference for the utilization of the geothermal resources in the Aba area.

2. Study Area

Western Sichuan is located at the eastern margin of the Tibetan Plateau [17–19]. The study area was the Aba area of western Sichuan, within the longitude of 100°30′–104°30′ and latitude of 30°35′–34°20′ (Figure 1). The complex topography of the Aba area leads to regional climate differences. The mounded plateau in the northwest has a continental plateau climate, with no significant difference in temperature. The mountainous plain has a cool and semi-humid climate, with distinct wet and dry seasons and vertical changes in climate. The high mountains are wet and cold, and the river valleys are dry and cool [20]. The annual precipitation and temperature are 741 mm and 12 °C, respectively. The landform is characterized by alpine and valley regions, with an average elevation of 3500–4000 m.

Tectonically, the Aba area is located in the Songpan–Ganzi geosyncline fold belt with a direction of 40°–50° from northeast to southwest. It is 156 km in length and 20–50 km in width [21]. NE- and NW-trending regional faults are developed in the Aba area. The Aba area is bounded by the Maqin–Lueyang fault in the north, by the Minjiang fault in the east, and it is separated by the Maowen fault in the southeast. The Aba area has experienced several periods of intense tectonic events. The complex structural system controls the patterns of strata extension, magmatic activity, and geothermal areas (Figure 1). The strata exposed in the geothermal area are listed in Table 1. According to the lithology and aquifer characteristics, the groundwater types are divided into three categories: the Quaternary pore water, bedrock fissure water, and karst water. The Quaternary pore water is mainly distributed in the Hong Yuan–Ruoergai grassland and river valley plain area within the aquifer of the sand and gravel layers. The clastic rock fissure water is distributed in the Wenchuan County within the aquifer of the Triassic and Jurassic sandstone and mudstone. It is mainly recharged by rainfall and discharged as springs with flows of 0.1–1 L/s. Karst water is distributed in the Devonian, Carboniferous, and Permian thick-layered dolomite and limestone. This type of groundwater is recharged by rainfall and snow and discharges as springs. The spring flow is generally 1–50 L/s. In general, the annual runoff is mainly recharged by atmospheric precipitation, the infiltration of alpine snowmelt, and groundwater runoff from deep circulation.

The distribution of geothermal resources in the Aba area is controlled by the faults in the region. Geothermal resources are mainly concentrated in the northeastern Songpan County and the southeastern Maoxian–Lixian–Wenchuan area. The geothermal resources in the Lixian County are mainly controlled by the Xuecheng S-type structure. The faults and secondary fractures are well developed in the geothermal area, providing a vital channel for the circulation of geothermal water. The exposed temperatures of the geothermal water range 23–48 °C. To date, they have been utilized for tourism and spa purposes.

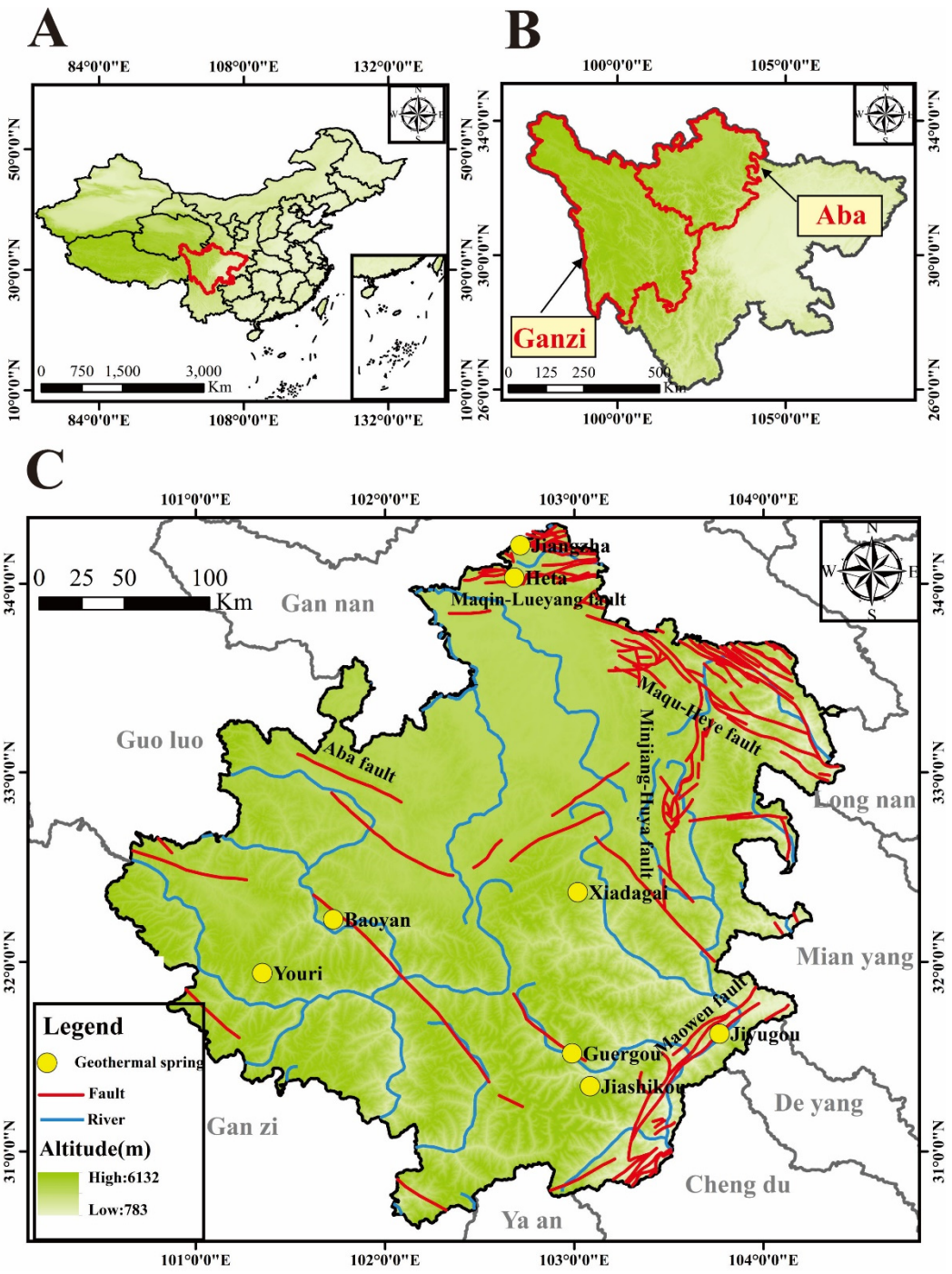

Figure 1. (**A**) Location of the Sichuan Province in China, (**B**) Location of the Ganzi and Aba region in the Sichuan Province, (**C**) Distribution map of the geothermal springs in the Aba area.

Table 1. Statistics of the hydrochemical parameters, main ions, and isotopes of the geothermal springs in the Aba area.

ID	Name	Altitude (m)	T (°C)	pH	TDS (mg/L)	Structural Location	Geothermal Reservoir Temperature Lithology
ABQ01	Heta	3360	30.49	7.6	264.80	Maqin–Lueyang deep fault zone	Conglomerate intercalated with metamorphic limestone
ABQ02	Jiangzha	3253	38.40	6.6	917.00	Maqin–Lueyang deep fault zone	Siliceous dolomite
ABQ03	Guergou	2583	48.00	8.9	190.40	The Miyaluo fault	Granite
ABQ04	Xiadagai	3402	35.00	8.4	222.90	Structure of Zhimulin Mountain type	Calcareous quartz sandstone
ABQ05	Baoyan	3360	48.00	7.1	530.70	Caodeng syncline	Slate, phyllite
ABQ06	Jiashikou	2840	44.00	9.1	298.30	Xuecheng S-type structure	Conglomeratic sandstone
ABQ07	Jiyugou	1703	31.92	7.1	937.40	Maowen active fault	Metamorphic dolomite
ABQ08	Youri	3920	23.00	9.5	227.40	The Seda fault, Rushi anticline and Balachon syncline	Sandstone

ID	K^+	Na^+	Ca^{2+}	Mg^{2+}	Cl^-	SO_4^{2-}	HCO_3^-	CO_3^{2-}	H_2SiO_3	Sr	F	Li	B	$\delta^{18}O$	δD	Re
ABQ01	1.40	8.00	46.09	27.36	0.35	32.48	247.10	0.00	43.64	0.14	0.47	0.02	1.05	−13.58	−96.2	4960
ABQ02	8.00	50.00	173.3	71.14	3.90	209.60	726.10	0.00	59.20	1.26	1.04	0.19	2.35	−13.88	−100.4	5015
ABQ03	1.60	29.00	6.01	0.61	2.48	14.16	66.02	3.05	116.81	0.04	1.39	0.02	0.49	−16.38	−118.6	5040
ABQ04	1.40	54.00	6.01	0.61	7.45	27.60	79.32	30.01	93.18	0.02	7.84	0.05	1.01	-	-	-
ABQ05	12.00	160.00	12.02	0.61	12.00	11.92	482.00	0.00	164.55	0.35	12.00	2.23	7.09	-	-	-
ANQ06	1.30	75.00	4.01	1.22	5.32	12.44	79.32	54.01	100.49	0.058	0.01	0.072	1.65	-	-	-
ABQ07	6.00	30.00	170.30	72.35	9.57	516.00	292.90	0.00	42.32	4.56	2.18	0.06	1.13	−12.20	−85.1	2876
ABQ08	1.00	46.00	2.00	0.61	3.90	8.16	90.03	15.25	55.90	0.03	5.37	0.05	0.36	-	-	-
ABD09	1.45	17.10	59.90	10.40	1.80	55.30	221.90	3.00	11.00	0.33	0.11	0.05	0.10	-	−54.60	-

Notes: pH has no unit. The unit for TDS, K^+, Na^+, Ca^{2+}, Mg^{2+}, Cl^-, SO_4^{2-}, HCO_3^-, CO_3^{2-}, H_2SiO_3, Sr, B, F, and Li is mg/L; the unit for $\delta^{18}O$ and δD is ‰VSMOW; "-" indicates no data. Re represents the recharge elevation (m). ABD09 represents the surface water sample.

3. Sample Collection and Laboratory Experiment

In this study, eight geothermal spring and one surface water body were sampled in the Aba area during August 2013. The German Multi 3630 IDS portable multi-parameter device was used for the field measurements. Water samples were filtered through a 0.45 μm filter membrane and then sealed in polyethylene plastic bottles. The in situ measurement parameters included water temperature, total dissolved solids (TDS), and pH value. The collected samples were sent to the Chengdu Analytical & Testing Center for a hydrochemical analysis within one week. The hydrogen and oxygen isotope analysis was carried out at the Institute of Hydrogeology, Environmental Geology, Chinese Academy of Geological Sciences. The anions were analyzed using the ion chromatography technique (Dionex-500), and the cations were analyzed by using an inductively coupled plasma emission spectrometer (ICP-OES). The test accuracy of the ion analysis was controlled to be within 3%. Hydrogen and oxygen isotopes were detected by using wavelength scanning cavity ring-down spectroscopy at 23 °C and 50% humidity. The total analysis indexes of the geothermal springs' chemistry include the pH value, total dissolved solids (TDS), main anions (HCO_3^-, SO_4^{2-}, Cl^-, CO_3^{2-}), main cations (Na^+, K^+, Ca^{2+}, Mg^{2+}), and trace elements (F, Sr, Li, B, H_2SiO_3). The hydrochemical and D-O isotopic results are shown in Table 1.

4. Results and Discussion

4.1. General Hydrochemical Characteristics

A Piper diagram is helpful for revealing the major cations and anions in water and the differences in the hydrochemical type [22]. The chemical types of the geothermal springs in the Aba area were analyzed by a Piper diagram. As shown in Figure 2, the geothermal springs were classified into two groups: Ca-HCO_3-(SO_4) (class A) and Na-HCO_3 (class B). The geothermal springs ABQ01, ABQ02, and ABQ07 were classified as class A. The remaining five geothermal springs were classified as class B.

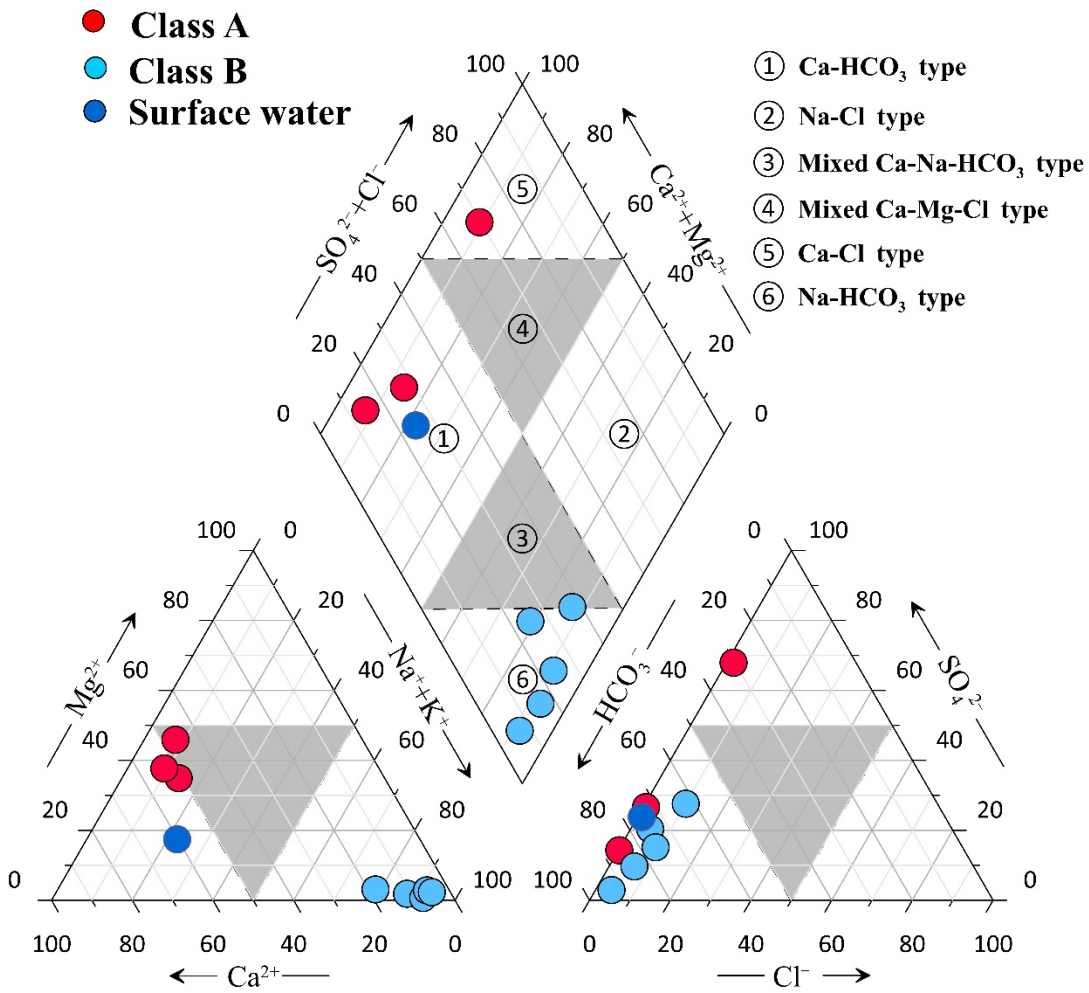

Figure 2. Piper trilinear diagram of the geothermal springs in the Aba area.

In this study area, the pH values of the geothermal springs in class A and B slightly changed. The pH values of class A ranged from 6.6 to 7.6, while class B ranged from 7.1 to 9.5, showing weak alkaline. According to the degree of mineralization, groundwater can be divided into five categories: fresh water (less than 1000 mg/L), brackish water (1000–3000 mg/L), salt water (3000–1000 mg/L), saline (10,000–50,000 mg/L), and brine (more than 50,000 mg/L). As shown in Figure 3A,B, the total dissolved solids (TDS) content of class A and B geothermal springs varied from 264.80 to 937.40 mg/L (average = 706.40 mg/L) and from 190.40 to 530.70 mg/L (average = 293.94 mg/L), respectively; therefore, they belong to fresh water. The main cation concentrations of class A were ranked in the descending order of Ca^{2+} (average = 129.90 mg/L), Mg^{2+} (average = 56.95 mg/L), Na^{+} (average = 29.33 mg/L), and K^{+} (average = 5.13 mg/L). Ca^{2+} and Mg^{2+} accounted for 58.69% and 25.73% of the total, respectively. The main cation concentrations of class B followed the descending order of Na^{+} (average = 72.80 mg/L), Ca^{2+} (average = 6.01 mg/L), K^{+} (average = 3.46 mg/L), and Mg^{2+} (average = 0.73 mg/L). The dominant cation was Na^{+}, accounting for 87.71% of total cations. The main anion concentrations of class A geothermal springs were in the descending order of HCO_3^{-} (average = 422.03 mg/L), SO_4^{2-} (average = 252.69 mg/L), and Cl^{-} (average = 4.61 mg/L), respectively. the anions were mainly HCO_3^{-} and SO_4^{2-}, which accounted for 62.12% and 37.20% of the total, respectively. The main anion concentrations of class B were the same as those of class A geothermal spring, and the average concentrations were measured at 159.34, 14.86, and 6.23 mg/L, respectively. HCO_3^{-} was the main anion, accounting for 88.31% of the total.

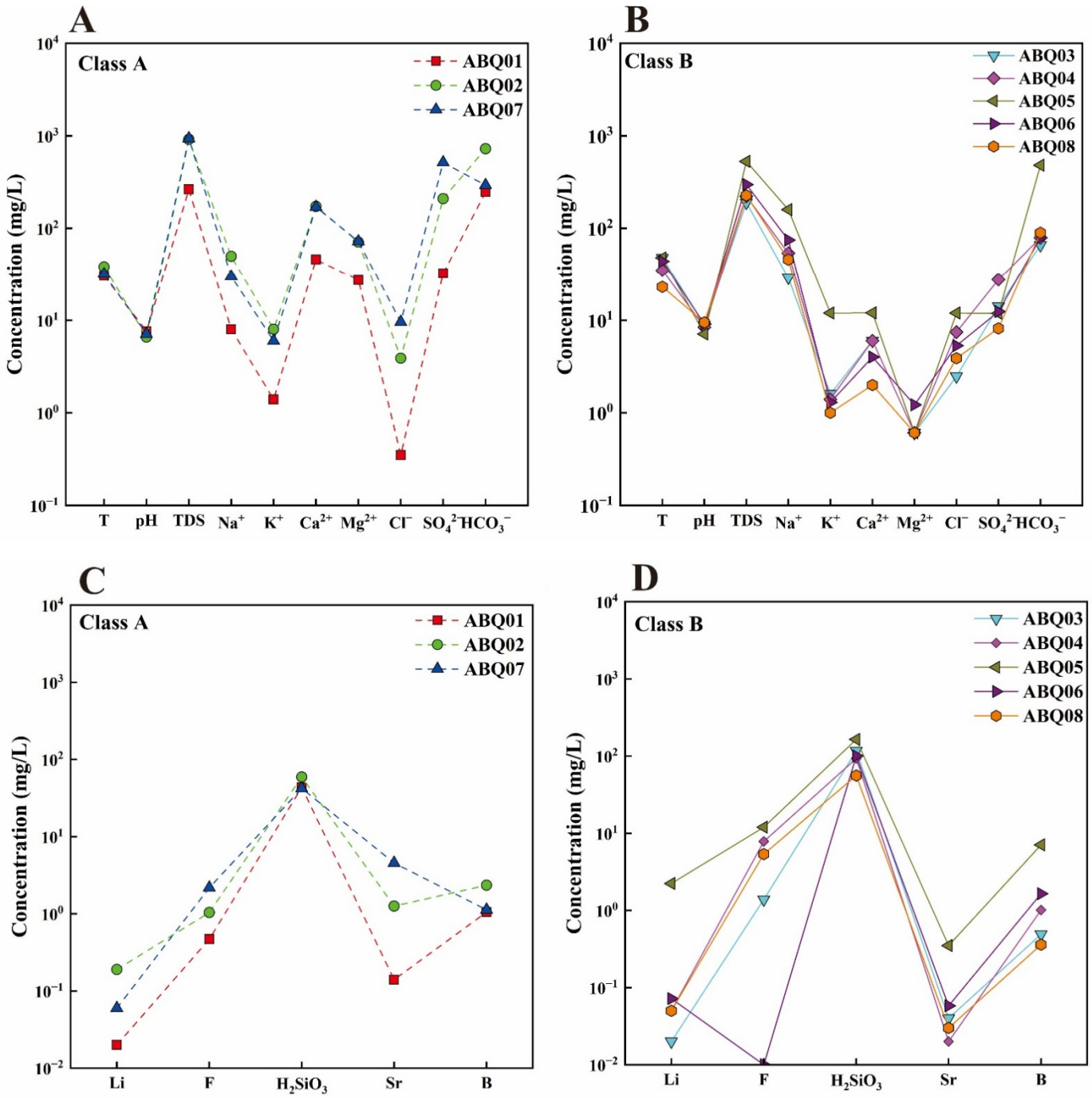

Figure 3. Concentrations of the major elements of the Class A (**A**) and Class B (**B**) geothermal springs of the Aba area. Concentrations of the trace elements of the Class A (**C**) and Class B (**D**) geothermal springs of the Aba area.

As shown in Table 1, Figure 3C,D also show that the concentration of trace elements of class A followed the order of H_2SiO_3 > Sr > B > F > Li. The concentration of H_2SiO_3 was 42.31–59.20 mg/L, and the average concentration was 48.38 mg/L. Sr concentration was 0.14–4.56 mg/L, with an average concentration of 1.99 mg/L. Class B concentration was 1.05–2.35 mg/L, with an average concentration of 1.51 mg/L. F concentration was 0.47–2.18 mg/L, with an average concentration of 1.23 mg/L. Li concentration was 0.02–0.19 mg/L, with an average concentration of 0.09 mg/L. The concentration order of trace elements in class B was in the order of H_2SiO_3 > F > B > Li > Sr. The concentration of H_2SiO_3 was 55.89–164.56 mg/L, with an average concentration of 106.19 mg/L. F

concentration was 0.01–12 mg/L, with an average concentration of 5.32 mg/L. B concentration was 0.36–7.09 mg/L, with an average concentration of 2.12 mg/L. Li concentration was 0.02–2.23 mg/L, with an average concentration of 0.48 mg/L. Sr concentration was 0.02–0.35 mg/L, with an average concentration of 0.10 mg/L. The H_2SiO_3 content in class B was higher than that in class A, but the Sr content in class B was lower than in class A. There was no obvious regular change in the trace element content between geothermal springs in different regions. The contents of trace elements in different regions of class B geothermal springs were the same, but the F ion content of the ABQ05 geothermal spring in class B was significantly higher than that of ABQ06 (Figure 3D).

4.2. Factors Controlling Hydrochemical Compositions

4.2.1. Correlation Analysis of Each Parameter

(1) Correlation Analysis of Major Ions

The Pearson correlation coefficient matrix is a useful tool in hydrochemical analyses [23]. In this study, the Origin 2022 software was used to calculate the correlation coefficient matrix of the hydrochemical parameters, as shown in Figure 4. The correlation between each parameter was represented to analyze the relationship of the ion source [24].

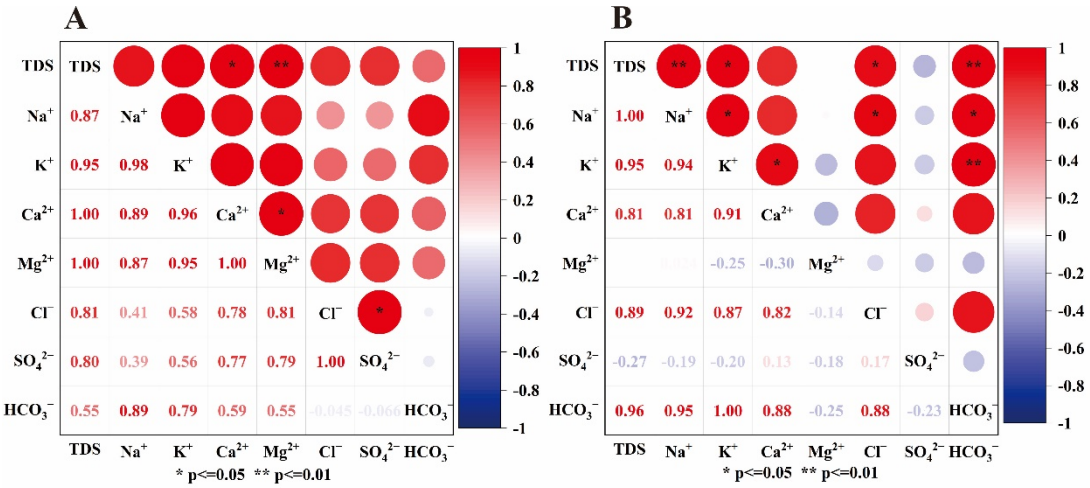

Figure 4. Correlation coefficient matrix of the class (**A**) (left) and class (**B**) (right) geothermal springs.

There was a significant positive correlation between the TDS and the Na^+, K^+, Ca^{2+}, Mg^{2+}, Cl^- and $SO_4{}^{2-}$ concentration in class A (Figure 4A). This suggested that the TDS was controlled by the Na^+, K^+, Ca^{2+}, Mg^{2+}, Cl^- and $SO_4{}^{2-}$ concentrations. The correlations between the TDS and Ca^{2+} and Mg^{2+} concentrations were the most significant, with values greater than 0.9. Hence, Ca^{2+} and Mg^{2+} were the main source of the TDS. Ca^{2+} and Mg^{2+} had high correlations with $SO_4{}^{2-}$ (0.767, 0.794), indicating that Ca^{2+}, Mg^{2+}, and $SO_4{}^{2-}$ might have the same source. The correlations of Ca^{2+}, Mg^{2+}, and $HCO_3{}^-$ indicated that the weathering of calcite and dolomite contribute a certain extent to the hydrochemical compositions of the surface and groundwater.

There were significant positive correlations between the TDS and the Na^+, K^+, Ca^{2+}, Mg^{2+}, Cl^-, and $HCO_3{}^-$ concentrations in Class B (Figure 4B). This indicated that the TDS was mainly controlled by the Na^+, K^+, Ca^{2+}, Mg^{2+}, Cl^-, and $HCO_3{}^-$ concentrations. The correlations between the TDS and the Na^+, K^+ and $HCO_3{}^-$ concentrations were the most significant, with correlation constants greater than 0.9, indicating that Na^+, K^+ and $HCO_3{}^-$ were the main sources of TDS. $HCO_3{}^-$ had significant correlations with K^+, Na^+, and Ca^{2+}, with correlation coefficients of 0.952, 0.996, and 0.878, respectively, indicating that it may mainly originate from silicate weathering [25]. Cl^- was well correlated with Na^+ and K^+, with correlation coefficients of 0.922 and 0.866, respectively, indicating the presence of evaporite dissolution in class B geothermal springs. Moreover, $HCO_3{}^-$ also showed

good correlation with Na^+ and K^+, with correlation coefficients of 0.952 and 0.996. We speculated that this was the case because the main anion of the geothermal spring in class B was HCO_3^- and the concentration of Cl^- was low. The ion ratio and a saturation index were used to further prove the relationship among the major ions after these findings.

(2) Correlation Analysis of Trace Element

In geo-environments, Cl^- has difficulty forming minerals with other cations or being adsorbed to the surface of minerals, even in high temperature and pressure conditions. Based on the stability of Cl^-, it was widely used to trace the ion source in the geothermal water [26–28].

In the class A geothermal springs, the Cl^- concentration was well correlated with that of Sr, Li, and F (Figure 5). In the class B geothermal springs, the Cl^- concentration had a good relationship with Sr, Li, F, and B concentrations (Figure 5). This indicated that Li, B, and Sr were derived from the incorporation of mantle source components [29], and that the class B type Baoyan geothermal spring (seen in Table 1) had high Cl^-, Li, B, and F ion contents, indicating more involvement of mantle source components. As shown in Figure 5, B and Cl^- showed a negative correlation, and the geothermal water with a higher B concentration had a lower Cl^- content, indicating that B and Cl^- had different material sources. Furthermore, B ions originated from the dissolution of minerals containing B in carbonates. Moreover, the positive correlation between Cl^- and Sr in class A was greater than in class B, indicating that the water–rock interaction is greater in class A than in class B. H_2SiO_3 in the geothermal springs mainly originated from the dissolution of silicate minerals, which was different from the source of Cl^-; class A Cl^- and H_2SiO_3 showed a negative correlation and class B did not show an obvious linear relationship. The higher the temperature of the deep geothermal reservoir temperature, the higher the H_2SiO_3 content of the geothermal water. By contrast, during the upward transport of geothermal water to the surface, H_2SiO_3 does not precipitate in large quantities due to the decrease in temperature. Therefore, the SiO_2 content was used to calculate the geothermal reservoir temperature [30]. The average H_2SiO_3 concentration of class B was higher than that of class A, indicating that the geothermal reservoir temperature of class B geothermal spring was rich in silicate minerals and that the geothermal reservoir temperature was high.

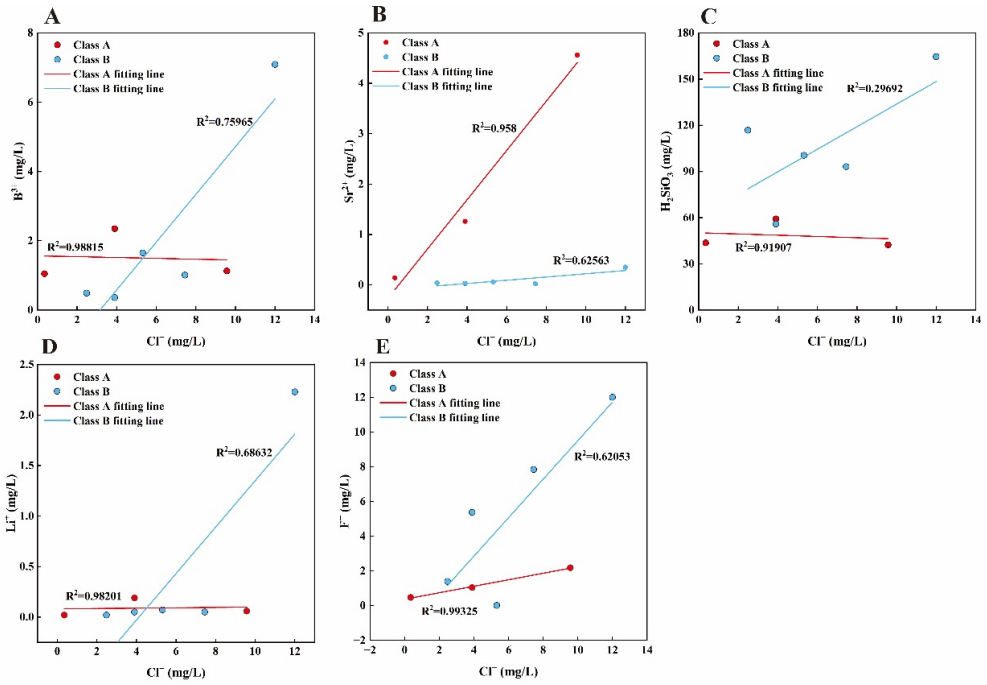

Figure 5. Relationship between the trace elements and the chlorine content. (**A**) Cl^- vs. B^{3+}, (**B**) Cl^- vs. Sr^{2+}, (**C**) Cl^- vs. H_2SiO_3, (**D**) Cl^- vs. Li^+, (**E**) Cl^- vs. F^-.

4.2.2. Analysis of Ion Ratios

The ratio of major ions can further determine the processes affecting the hydrochemical characteristics. A Gibbs diagram was used to reflect the controlling factors of the major ions in water (precipitation, water–rock interaction, and evaporation) [31]. Figure 6A,B show the Gibbs plot of the geothermal springs in the Aba area. The results showed that the major ion compositions of class A and B geothermal springs in the Aba area were mainly affected by the water–rock interaction. In Figure 6A, the $Na^+/(Na^+ + Ca^{2+})$ value of the class B sample was close to 1 and was located on the right end of the rock dominance. This indicates that cation exchange may occur in class B geothermal springs. This is because there may be hydrolysis and acid action in the geothermal springs during runoff, which would cause the release of Na^+ during the weathering of silicate rocks, and an exchange with Ca^{2+} in the water, resulting in an increase in Na^+ concentration.

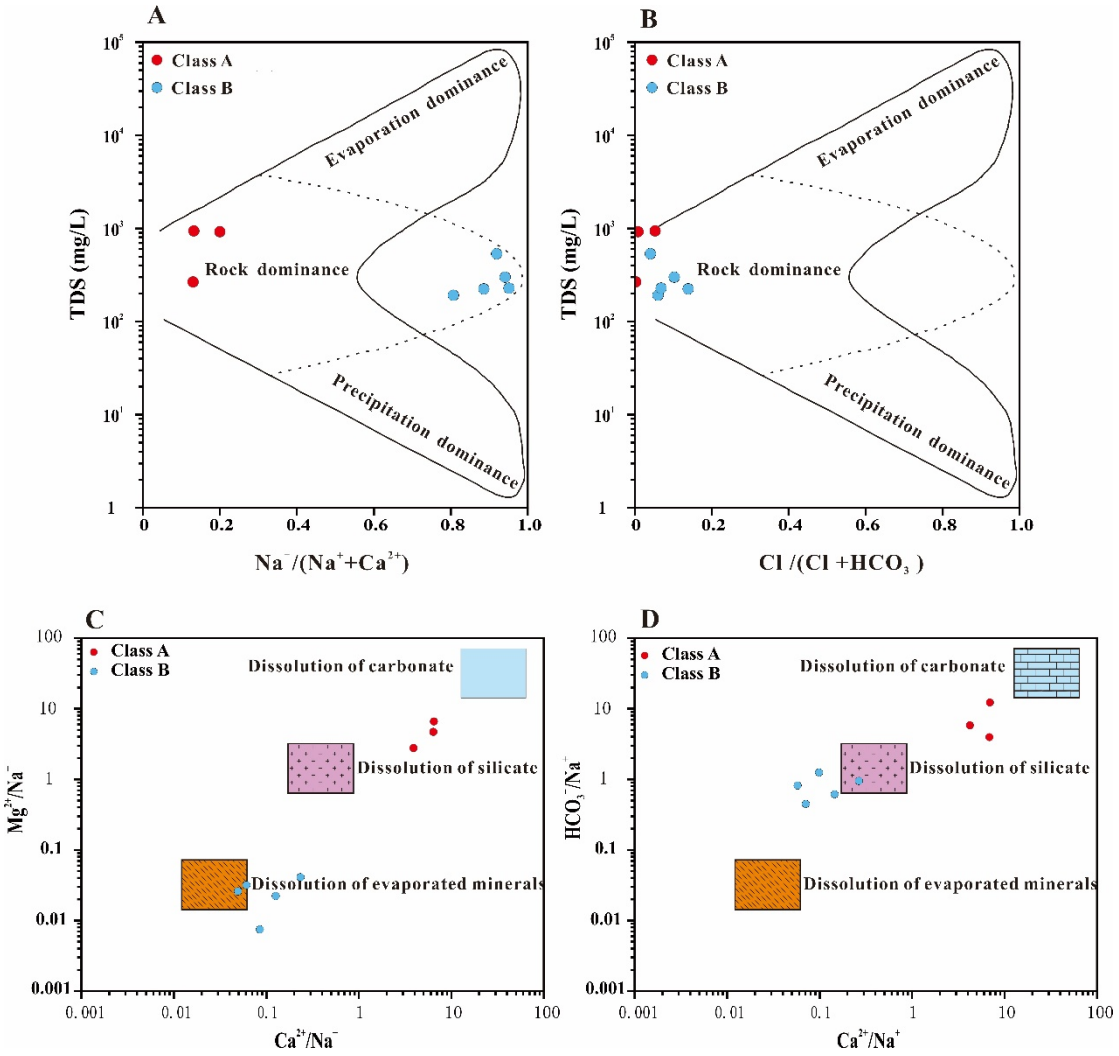

Figure 6. Gibbs diagram of (**A**) TDS vs. $Na^+/(Na^+ + Ca^{2+})$ and (**B**) TDS vs. $Cl^-/(Cl^- + HCO_3^-)$. Ratio diagram of (**C**) Ca^{2+}/Na^+ vs. Mg^{2+}/Na^+ and (**D**) Ca^{2+}/Na^+ vs. HCO_3^-/Na^+.

Ca^{2+}/Na^+, Mg^{2+}/Na^+ and HCO_3^-/Na^+ ratios are commonly used to distinguish the type of water–rock interaction [22]. Figure 6C,D show that the class A geothermal springs were located between silicate weathering and carbonate dissolution, while the class B geothermal springs were located in evaporite and silicate dominance. We propose that the weathering and dissolution of silicate and carbonate indicate that evaporite and silicate were the main mineral types of the water–rock interaction.

Hence, the hydrochemical compositions of the geothermal springs in the Aba were determined by the water–rock (carbonate, evaporite, and silicate) interaction. The major ion ratio is often used to further reveal the mineral weathering and dissolution involved in the hydrogeochemical processes [28,32,33].

(1) $(K^+ + Na^+)/Cl^-$

The molar ratio relationship between $(K^+ + Na^+)$ and Cl^- is commonly used to reveal the source of Na^+ and K^+ in groundwater [34]. As shown in Figure 7A, both class A and B geothermal springs fell below the y = x line and close to the axis with respect to $K^+ + Na^+$. This indicates that the Cl^- of class A and B geothermal springs were not enough to balance K^+ and Na^+. Excess Na^+ and K^+ concentrations may originate from the weathering dissolution of silicate minerals, such as sodium feldspar, potassium feldspar, and other silicate minerals (Formula (1) and (2)). In Figure 4, HCO_3^- had a significant correlation with K^+ and Na^+, which also indicates the weathering of potassium/sodium silicate minerals.

$$Na_2Al_2Si_6O_{16} + 2CO_2 + 3H_2O \rightarrow 2HCO_3^- + 2Na^+ + H_4Al_2SiO_9 + 4SiO_2 \quad (1)$$

$$K_2Al_2Si_6O_{16} + 2CO_2 + 3H_2O \rightarrow 2HCO_3^- + 2K^+ + H_4Al_2SiO_9 + 4SiO_2 \quad (2)$$

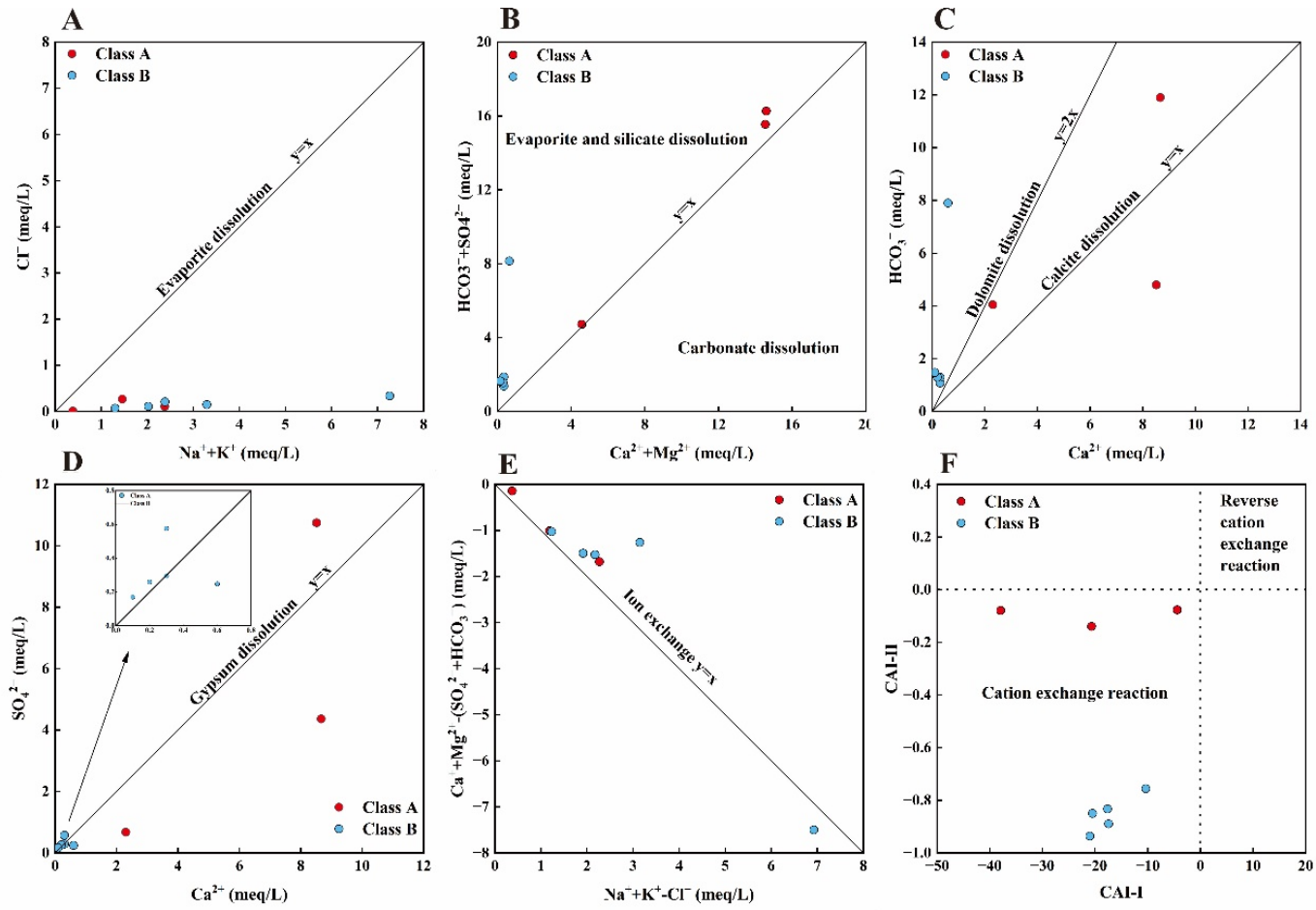

Figure 7. Molar ratio diagram of (**A**) Cl^- vs. $(Na^+ + K^+)$, (**B**) $(HCO_3^- + SO_4^{2-})$ vs. $(Ca^{2+} + Mg^{2+})$, (**C**) HCO_3^- vs. Ca^{2+}, (**D**) SO_4^{2-} vs. Ca^{2+}, (**E**) $(Na^+ + K^+ - Cl^-)$ vs. $(Ca^{2+} + Mg^{2+} - HCO_3^- - SO_4^{2-})$, (**F**) $(Cl^- - (Na^+ + K^+))/Cl^-)$ vs. $(Cl^- - (Na^+ + K^+))/(HCO_3^- + SO_4^{2-} + CO_3^{2-} + NO_3^-)$.

(2) $(Ca^{2+}+Mg^{2+})/(HCO_3^- + SO_4^{2-})$

The sources of Ca^{2+}, Mg^{2+}, HCO_3^-, and SO_4^{2-} in the groundwater are mainly from the dissolution of carbonates (calcite, dolomite) and sulfates (gypsum). The molar ratio

between (Ca^{2+} + Mg^{2+}) and (HCO_3^- + SO_4^{2-}) was used to determine the source of Ca^{2+} and Mg^{2+} [35]. When the samples are close to the molar ratio of 1:1, the dissolution of carbonate and silicate minerals is the main source of the Ca^{2+} and Mg^{2+} concentrations. When this ratio is much larger than the 1:1 dissolution line, the dissolution of carbonate minerals accounts for the Ca^{2+} and Mg^{2+} concentrations. When this ratio is much smaller than the 1:1, the dissolution of evaporite and silicate minerals is responsible for the Ca^{2+} and Mg^{2+} concentrations. As shown in Figure 7B, most class B geothermal springs deviated above the 1:1 line, indicating that Ca^{2+} and Mg^{2+} in class B geothermal springs mainly originated from evaporite dissolution and silicate weathering. Class A geothermal springs were mainly distributed near the y = x line, indicative of the existence of carbonate dissolution and silicate weathering.

(3) Ca^{2+}/HCO_3^-

When the molar ratio of Ca^{2+}/HCO_3^- is between 1:1 and 1:2, the source of Ca^{2+} and Ca^{2+} + Mg^{2+} concentrations is mainly derived from carbonate (calcite, dolomite) dissolution [36]. As shown in Figure 7C, two of the geothermal spring samples in class A fell between y = x and y = 2x, and only one fell below y = x, near the side of the Ca^{2+} axis. Excess Ca^{2+} concentration is attributed to the weathering of Ca-bearing silicate minerals. Class B geothermal springs were above the y = 2x line. The elevated concentration of HCO_3^- was caused by the weathering of potassium/sodium silicate minerals.

(4) Ca^{2+}/SO_4^{2-}

When the molar ratio between Ca^{2+} and SO_4^{2-} has a linear relationship of y = x, Ca^{2+} and SO_4^{2-} concentrations mainly originate from gypsum dissolution [37]. As shown in Figure 7D, the deviation from the y = x line for the class A geothermal springs indicate that gypsum dissolution is the dominant process. The excess SO_4^{2-} concentration in class A probably originates from hydrogen sulfide in the deep geothermal water. Class B geothermal springs were located close to the gypsum dissolution line. This suggests that gypsum dissolution exists in class B geothermal springs.

4.2.3. Ion Exchange Process

The ratio of (Ca^{2+} + Mg^{2+} − (SO_4^{2-} + HCO_3^-)) to (Na^+ + K^+ − Cl^-) can be used to evaluate the intensity of cation exchange [36]. When an ion exchange process exists, the relationship between (Ca^{2+} + Mg^{2+})–(SO_4^{2-} + HCO_3^-) and (Na^+ + K^+ − Cl^-) should be a linear correlation of −1. In Figure 7E, the class A and B geothermal springs followed the y = −x line. The linear of class A was −0.7991 and the R^2 value was 0.95282. The class B slope was −1.17332 and the R^2 value was 0.8801. Hence, ion exchange was determined to be the main process controlling the hydrochemistry in class A and B geothermal springs. The ion exchange interactions can also be further identified using the chlor-alkali index, where CAI-I = (Cl^- − (Na^+ + K^+))/Cl^- and CAI-II = (Cl^- − (Na^+ + K^+))/(HCO_3^- + SO_4^{2-} + CO_3^{2-} + NO_3^-) [38]. When both CAI-I and CAI-II are negative, it means that a cation exchange occurs. When CAI-I and CAI-II are positive, it indicates the presence of a reverse cation exchange. As shown in Figure 7F, class A and B geothermal springs possessed CAI-I and CAI-II values lower than zero, showing the occurrence of cation exchanges [36].

4.2.4. Mineral Saturation Index

The saturation index (SI) is important for measuring the equilibrium state of various minerals in water. Mineral equilibrium calculations can reflect the thermodynamic processes of natural water systems [39,40]. The SI values of minerals were calculated and evaluated using PHREEAC 3.0 software [32,41,42], based on Equation (3):

$$SI = \lg \frac{IAP}{K} \quad (3)$$

In Equation (3), SI is the mineral saturation index, IAP is the mineral-water reactivity, and K is the mineral-water equilibrium constant. When SI > 0, the solution is supersaturated

and the excess minerals will precipitate out; when SI < 0, the solution is unsaturated and the excess minerals will continue to dissolve; when SI = 0, the solution is in equilibrium and the minerals are dissolved and precipitated [22].

As shown in Figure 8, the SI values of calcite and dolomite were near zero and had reached saturation. The SI values of gypsum and halite were mainly below zero and had not reached saturation. Thus, calcite and dolomite dissolution were the main sources of water chemistry.

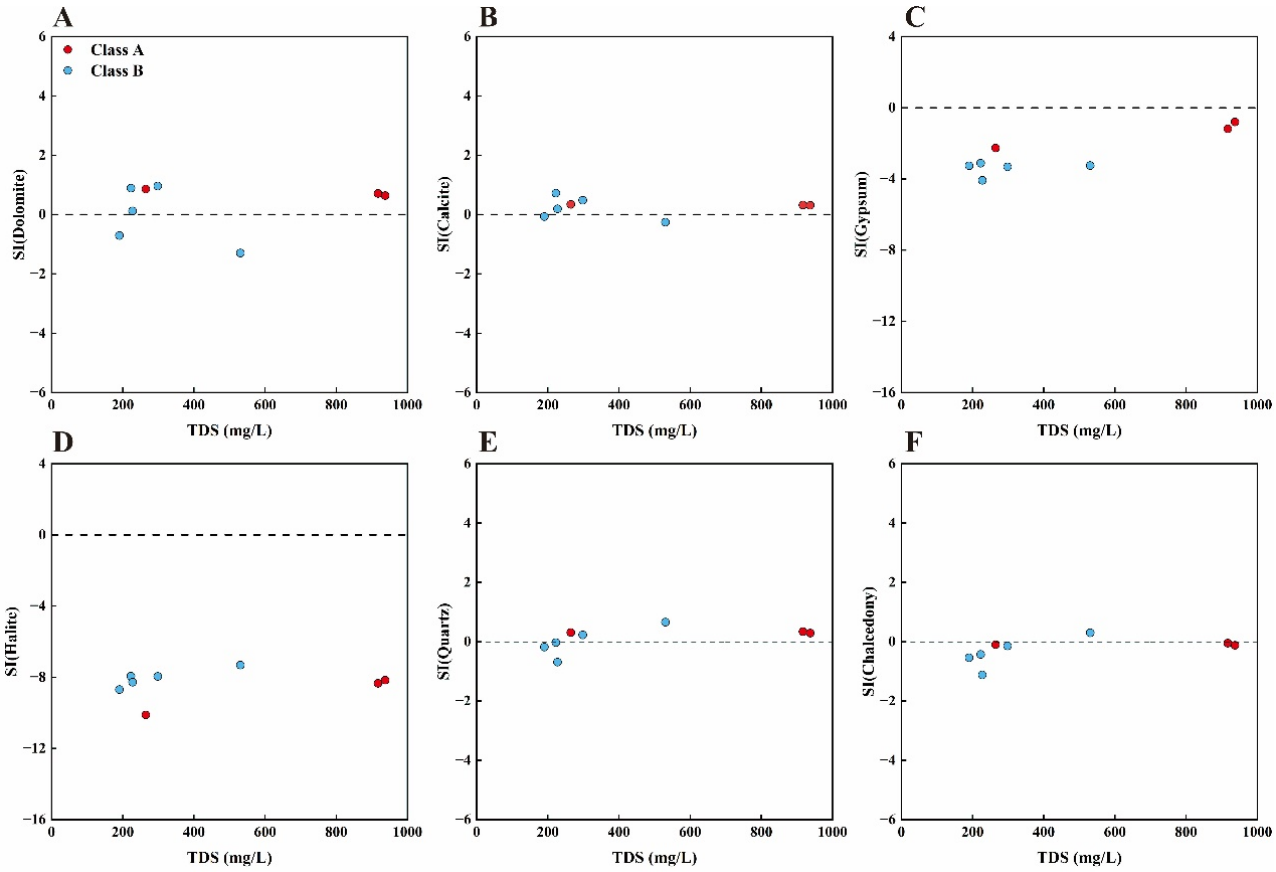

Figure 8. Relationship between the saturation index (SI) of different minerals and the total dissolved solids (TDS) in the studied geothermal springs. (**A**) SI (calcite); (**B**) SI (dolomite); (**C**) SI (gypsum); (**D**) SI (halite); (**E**) SI (quartz); and (**F**) SI (chalcedony).

4.3. Reservoir Characteristics of Geothermal System

4.3.1. Equilibrium State of Water–Rock Interaction

Prior to an estimation of the reservoir temperature using a geothermometer, it is necessary to evaluate the equilibrium state of water–rock interaction in geothermal water [43,44]. The Na-K-Mg triangle diagram was established to distinguish the equilibrium state from immature water, partial equilibration, and full equilibration [45]. In this study, class A and B geothermal springs belonged to immature waters (Figure 9A). Hence, a silica geothermometer was more suitable for estimating the reservoir temperature than a cation geothermometer for this study. SiO_2 solubility can be used to analyze the SiO_2 content that is controlled by various silica minerals (quartz, chalcedony, amorphous silica, etc.) in geothermal water [9]. Before calculating the geothermal reservoir temperature using a SiO_2 geothermometer, it is necessary to select the saturated SiO_2 minerals.

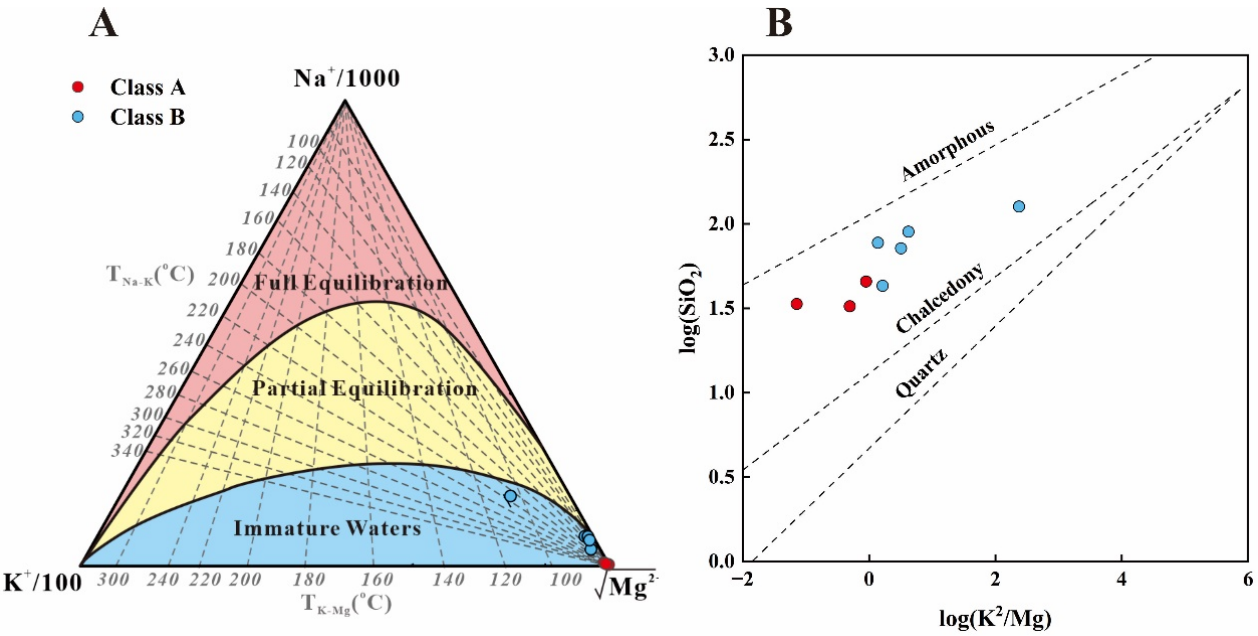

Figure 9. Na-K-Mg triangle diagram of the geothermal spring water in the Aba area [45]. (**A**); Discrimination diagram of SiO_2 mineral dissolution (**B**).

There are many kinds of silica minerals in nature, such as quartz, chalcedony, and amorphous silica, which are commonly involved in geothermal studies [46]. The equilibrium state of different SiO_2 minerals in geothermal water was analyzed in Figure 9B. Both class A and B fell above the chalcedony dissolution line. Furthermore, quartz (SI value = −0.69 to 0.66) was oversaturated and chalcedony (SI value = 1.12 to 0.3) was basically saturated in geothermal water (Figure 8E,F). Finally, the chalcedony geothermometer was chosen for the calculation of the reservoir temperature.

4.3.2. Reservoir Temperature Estimation

The equations for the silica geothermometers and cationic geothermometers are shown in Supplementary Table S1.

The reservoir temperatures of the geothermal springs in the Aba area are shown in Table 2. The geothermal reservoir temperature of chalcedony (maximum steam loss) in the class A geothermal springs ranged from 59.70 to 73.00 °C, with an average value of 64.53 °C. The geothermal reservoir temperature of chalcedony (maximum steam loss) in the class B geothermal spring ranged from 70.65 to 120.91 °C, with an average value of 96.70 °C. Overall, the geothermal reservoir temperature of class B was higher than that of class A. Class A geothermal springs were located near the fault zone, indicating that class A geothermal springs may have larger cold water mixing.

Geothermal water would be mixed with cold water on the surface in circulation. Because the geothermal springs in the study area have been proven to be affected by the shallow cold water, the silicon-enthalpy mixing model and equation were used to estimate the proportion of mixed cold water and initial geothermal reservoir temperature before the mixing [47,48]. The relationship between the temperature and the saturated enthalpy of water can be found in Supplementary Table S2. The surface water sample displayed a temperature of 10.78 °C and SiO_2 content of 8.46 mg/L.

Table 2. Calculation results of the geothermal temperature scale and cationic geothermal temperature scale of SiO_2, as well as the calculation results of the mixed model.

ID	T (°C)	Quartz [1]	Chalcedony [1]	Na-K	K-Mg	Na-K-Ca
ABQ01	30.49	87.16	60.88	257.22	19.00	7.02
ABQ02	38.40	98.83	73.00	244.73	41.94	41.18
ABQ03	48.00	127.75	103.43	131.52	57.75	53.36
ABQ04	35.00	117.65	92.25	77.20	54.90	110.29
ABQ05	48.00	144.11	120.91	158.75	107.78	126.34
ABQ06	44.00	120.97	96.25	53.80	46.22	64.36
ABQ07	31.92	86.03	59.70	276.99	36.26	29.96
ABQ08	23.00	96.57	70.65	66.57	47.92	65.52

ID	Silicon-Enthalpy Equation		Silicon-Enthalpy Diagram		Initial Silica Concentration (mg/L)
	Cold Water Mixing Ratio (%)	Geothermal Reservoir Temperature (°C)	Cold Water Mixing Ratio (%)	Geothermal Reservoir Temperature (°C)	
ABQ01	89.52	196.11	89.44	197.44	246.26
ABQ02	85.78	201.41	85.76	204.73	268.84
ABQ03	87.18	285.18	87.39	305.98	653.97
ABQ04	-	-	-	-	-
ABQ05	-	-	-	-	-
ABQ06	87.55	266.16	87.55	277.31	560.77
ABQ07	87.93	184.26	87.00	178.46	189.16
ABQ08	-	-	-	-	-

Note: Quartz [1] and Chalcedony [1] represent the maximum steam loss.

According to the silicon-enthalpy formula, we present the functional relationships between the enthalpy, SiO_2 content, and temperature (Figure 10). The intersection point indicates the proportion of mixed cold water and initial geothermal reservoir temperature. Regarding class A geothermal springs, the proportion of mixed cold water and initial geothermal reservoir temperature were 85.78–89.52% and 184.26–201.41 °C, respectively (Table 2). The proportion of mixed cold water and initial geothermal reservoir temperature in class B were 87.18–87.55% and 266.16–285.18 °C, respectively (Table 2).

The silicon-enthalpy diagram method was achieved based on the enthalpy and SiO_2 content of cold water (Figure 11). The initial temperature and geothermal water ratio (AB/AC) can be obtained by dropping point B according to the enthalpy of geothermal spring and SiO_2 content and by making the extension lines from A and B to point C [8]. The initial reservoir temperatures of the class A geothermal springs obtained by the silica-enthalpy diagram were 178.46–204.73 °C, with a cold water mixing ratio between 85.76 and 89.44%. The initial reservoir temperatures and cold water mixing ratio of the class B geothermal springs were 277.31–305.98 °C and 87.39–87.54% (Table 2), respectively. Herein, the average initial reservoir temperatures were calculated as 184.26–201.41 °C for class A and 266.166–285.18 °C for class B. The geothermal reservoir temperature could not be obtained using the silicon-enthalpy method for the ABQ04, ABQ05, and ABQ08 geothermal springs as there was no intersection point of the curves in Figures 10 and 11. We speculated that the geothermal water did not reach the chemical equilibrium. Generally, these three geothermal springs had lower geothermal reservoir temperatures.

By combining the results of the above multi-mineral equilibrium method, geothermometer, and silica-enthalpy mixing model calculations, we determined the reservoir temperature of the geothermal springs in the Aba area. The class A geothermal springs in the Aba area were located in the southeast and north of the Aba area. The results of the chalcedony (maximum steam loss) geothermometer measured temperatures ranging 59.70 °C–73.00 °C. The class B geothermal springs in the Aba area were located in the

central and southwest of the Aba area. The chalcedony (maximum steam loss) geothermal reservoir temperature range was 70.65–120.91°C. The initial reservoir temperatures were 184.26–201.41 °C for class A and 266.166–285.18 °C for class B, respectively. The reservoir strata of the class A geothermal springs are carbonate and metamorphic rocks, while for class B geothermal springs they are sand slate and Yanshanian igneous rocks. Therefore, the higher reservoir temperature of class B geothermal springs should be ascribed to the excess radioactive heat of the Yanshanian igneous rocks.

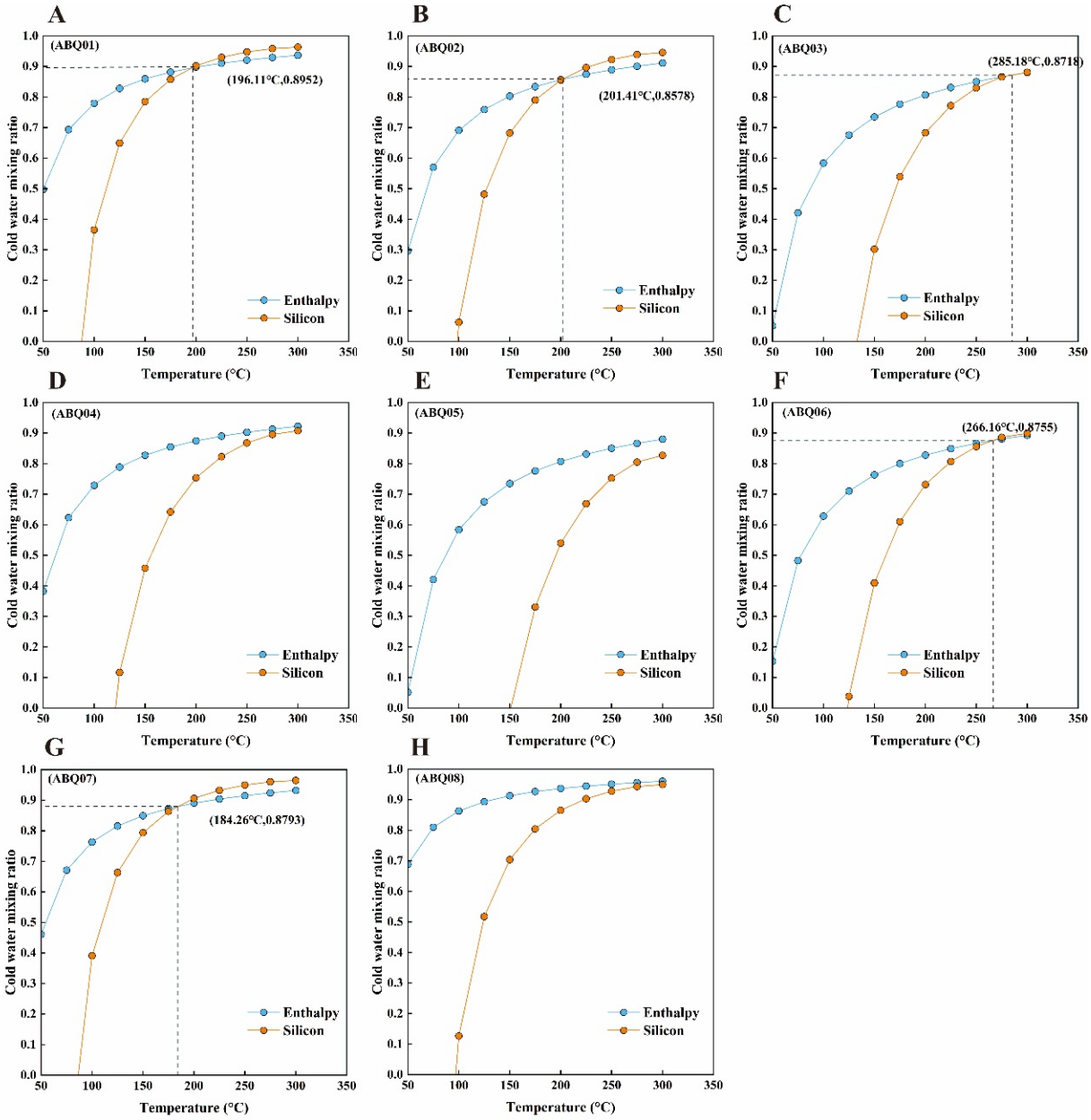

Figure 10. Silicon-enthalpy model diagram of the (**A**) ABQ01, (**B**) ABQ02, (**C**) ABQ03, (**D**) ABQ04, (**E**) ABQ05, (**F**) ABQ06, (**G**) ABQ07, (**H**) ABQ08 geothermal springs in the Aba area.

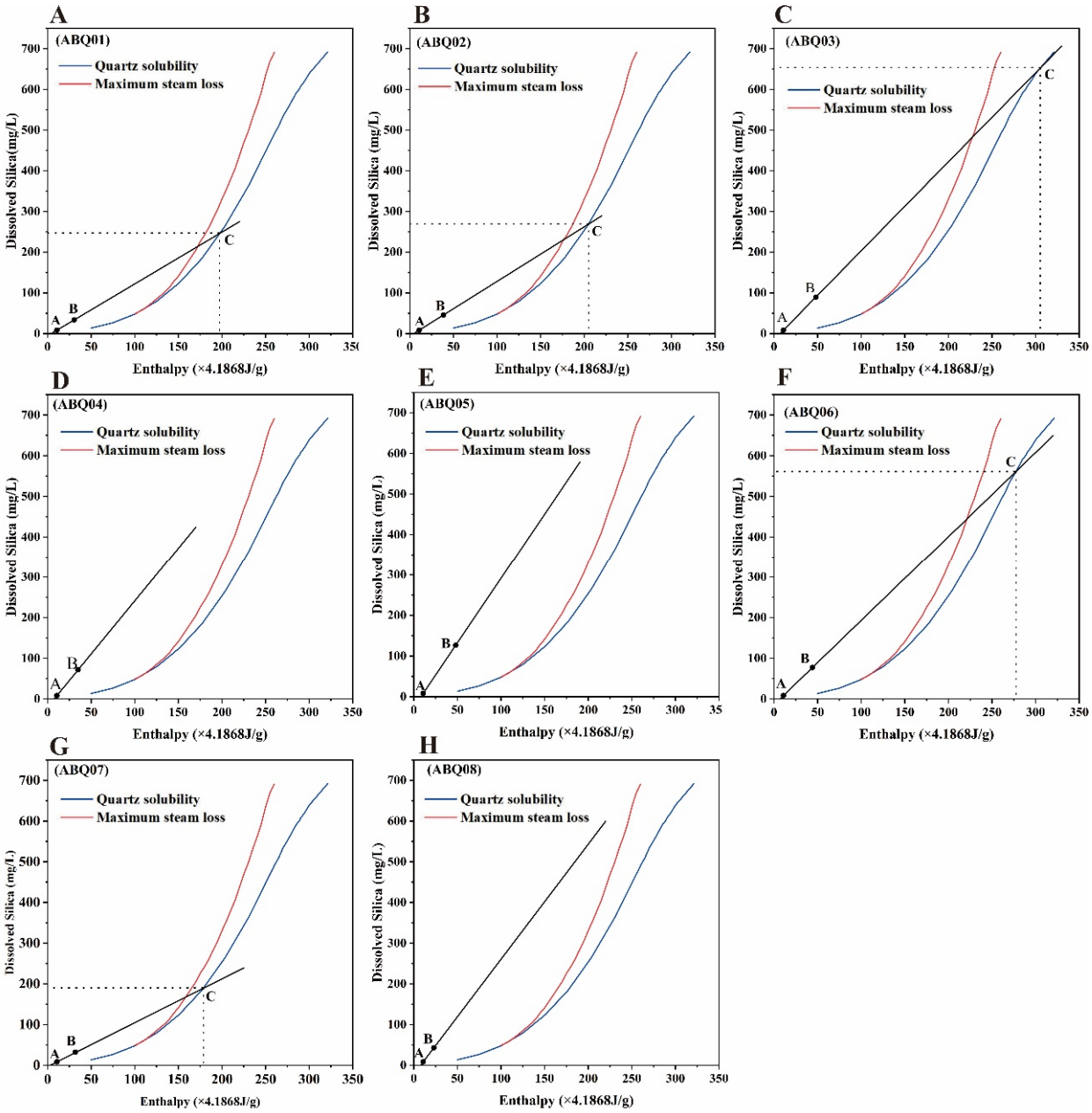

Figure 11. Solution diagram of the silicon-enthalpy diagram of the (**A**) ABQ01, (**B**) ABQ02, (**C**) ABQ03, (**D**) ABQ04, (**E**) ABQ05, (**F**) ABQ06, (**G**) ABQ07, (**H**) ABQ08 geothermal springs in the Aba area.

4.4. Recharge Origin of Geothermal Springs by D-O Isotopes

D-O isotopes are effective tracers for identifying recharge sources [49]. In this study, the recharge elevation was calculated by using D-O isotopes. The study conducted by Craig obtained the global meteoric water line (GMWL): $\delta D = 8\delta^{18}O + 10$ by the δD and $\delta^{18}O$ values of more than 400 natural water samples worldwide [50]. The linear relationship between the hydrogen and oxygen isotopes of the southwest meteoric water in China was clarified as $\delta D = 8.41\delta^{18}O + 16.72$ [51]. We analyzed the δD and $\delta^{18}O$ values of the geothermal springs in the study area (Table 1). The δD values of geothermal springs in the Aba area ranged from −118.6‰ to -85.1‰, with an average value of −100.08‰; $\delta^{18}O$ values ranged from −12.20‰ to −16.38‰, with an average value of −14.01‰. The δD value of surface water was −54.6‰. δD and $\delta^{18}O$ values of geothermal springs were lower

than those of the surface water, indicating higher recharge elevations and longer runoff pathways.

As shown in Figure 12, most of the δD and $\delta^{18}O$ values of the geothermal springs followed the local meteoric water line (LMWL) and the global meteoric water line (GMWL). This implies that the geothermal springs in the study area are recharged by atmospheric precipitation. Among the springs, ABQ01, ABQ03, and ABQ07 were located on the left side of the local meteoric water line (LMWL). Their deuterium excesses (D_{excess}) were 12.01‰, 11.92‰, and 12.11‰ higher than the average deuterium excesses of global meteoric water (10‰). It may be because these geothermal springs are partially recharged by ice melt, and thus kinetic fractionation has occurred during the ice melt. This would result in a higher proportional balance of ^{2}H and ^{18}O in the meltwater.

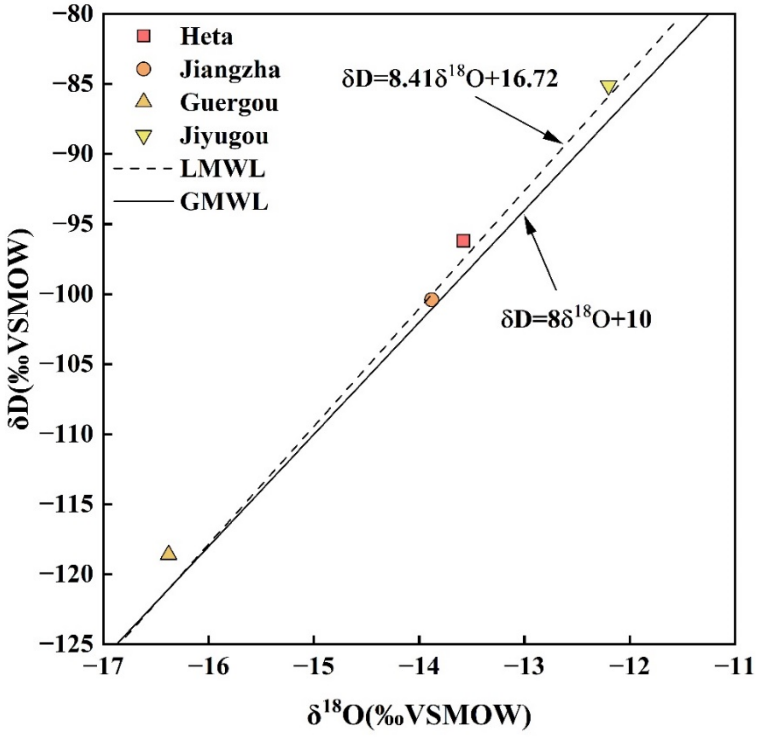

Figure 12. δD–$\delta^{18}O$ relation of the geothermal springs in the Aba area.

The δD and $\delta^{18}O$ values of the inland atmospheric precipitation have an elevation effect that decreases with an increase in topographic elevation. It is noteworthy that the "oxygen drift" is weak in Figure 12. Accordingly, the groundwater recharge area and recharge elevation can be estimated by the δD and $\delta^{18}O$ values. Formula (4) [52] for the geothermal spring recharge elevation in Aba area is:

$$H = \frac{\delta_G - \delta_P}{K} \times 100 + h \quad (4)$$

Equation (4): H, the recharge elevation of the geothermal spring (m); h, sampling point elevation (m); $\delta_G - \delta_P$, value of the spring (‰); δ_P, value of δ_D in surface water (‰); K, isotope elevation gradient (‰/100 m), this time taking −2.6‰/100 m [53].

The δ_D value of the surface water in the Aba area was taken as −54.6‰ (based on the existing surface rainfall isotope test data in the region). The recharge elevation of each of the three groups of geothermal springs was calculated by using the equation above (Table 1). As shown in Table 1, it can be seen that the geothermal spring recharge elevation in the Aba area was 2876–5040 m, with an average elevation of 4473 m.

4.5. Conceptual Genetic Model of Geothermal Springs in Aba Area

4.5.1. Carbonate Rock Area with Deep Fault (Class A)

Class A geothermal springs are developed in carbonate rock areas with deep faults. The representative sample is ABQ07 (Jiyugou), which was exposed in the Maowen fault. The geothermal reservoir was dominated by Cambrian siliceous dolomite, Holocene conglomerate intercalated with metamorphic tuff, and Sinian metamorphic dolomite (Table 1). There was no developed magmatic intrusion beneath. The geothermal springs are mostly distributed in the fault zone. The geothermal spring was mainly recharged by rainfall and snow melt water. The elevation difference formed a huge hydrostatic pressure, resulting in the geothermal water being heated by deep circulation. A conceptual genetic model of the class A geothermal springs is shown in Figure 13A.

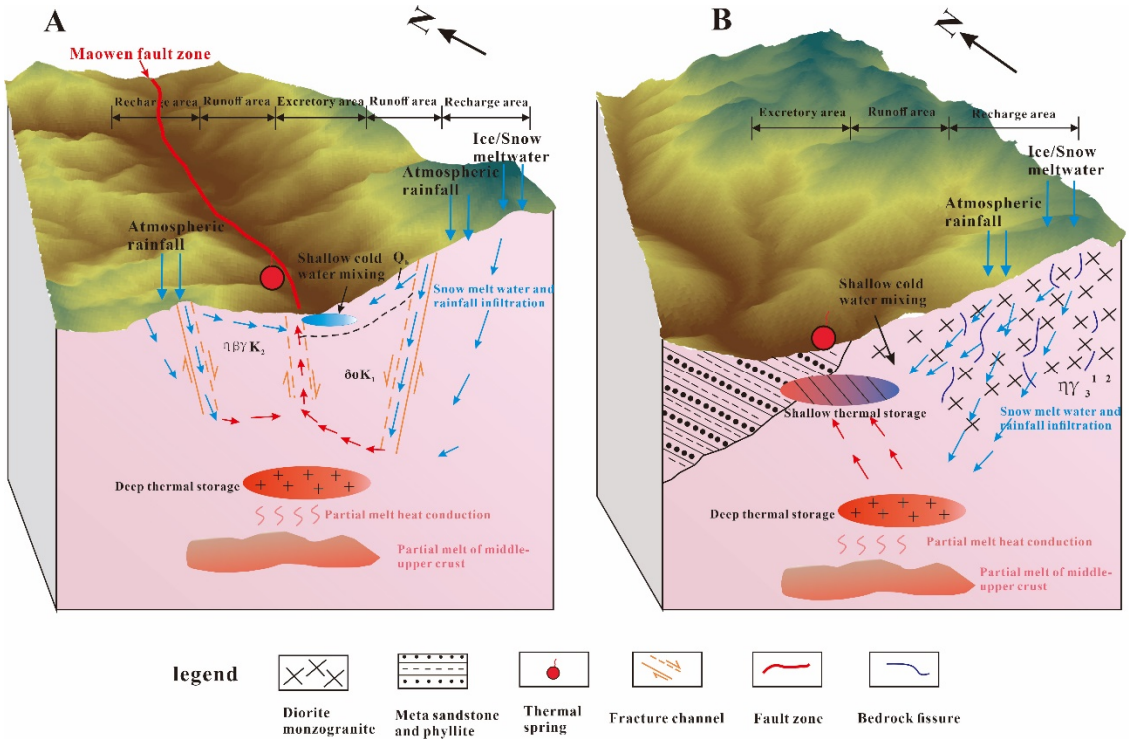

Figure 13. (**A**) Genetic model of the fault control type of the deep and large faults in the carbonate rock area. (**B**) Contact type genetic model of the magmatic residual heat intrusion zone.

4.5.2. Igneous Rock Area with Deep Fault (Class B)

Class B geothermal springs are formed in igneous rock areas with deep faults. The representative sample is ABQ03 (Guergou geothermal spring) (Table 1). This type was mainly distributed in the Maowen–Danba anticline and Maerkang syncline zones. The distribution characteristics of the geothermal springs were controlled by regional folding and fracture structures and were exposed in the Yanshanian igneous rocks with high contents of U, Th, and K [54]. The geothermal reservoir was dominated by Triassic sand slate strata and Yanshanian igneous rocks (Table 1). The fault and secondary fracture provided conditions for the storage, migration, and heat conduction of the geothermal water. The recharge area of the ABQ07 geothermal spring may be located in the Xuelongbao (5227 m) area. After being recharged by precipitation, groundwater seeped into the ground along rock fissures. Furthmore, it was gradually heated by the geothermal gradient and radioactive heat of the Yanshanian igneous rocks. A geothermal reservoir genesis model is shown in Figure 13B [55,56].

5. Conclusions

Eight geothermal springs were collected from the Aba area, Sichuan Province. Two classes divided the geothermal springs by their hydrochemical compositions: class A and class B. The main cations of class A geothermal springs followed the order of $Ca^{2+} > Mg^{2+} > Na^{+} > K^{+}$, and the anions followed the order of $HCO_3^{-} > SO_4^{2-} > Cl^{-}$. The class A geothermal spring belonged to the hydrochemical type of Ca-Mg-HCO_3-SO_4 and Ca-Mg-HCO_3. The main cations of class B followed the order of $Na^{+} > Ca^{2+} > K^{+} > Mg^{2+}$, and the anions followed the order of $HCO_3^{-} > SO_4^{2-} > Cl^{-}$. The hydrochemical type of class B geothermal spring was Na-HCO_3. The hydrochemical components of class A and B geothermal springs in the Aba area were mainly affected by the water–rock interaction. The ion concentrations of class A geothermal springs were determined by the weathering and dissolution of carbonate and silicate in cation exchange processes. The ion concentrations of class B geothermal springs were influenced by the weathering and dissolution of silicate and evaporite rocks in cation exchanges. Both class A and B geothermal springs belonged to immature water. The chalcedony geothermometer proposed that the class A shallow geothermal reservoir temperature was 59.70–73.00 °C (mixed by 85.76–89.44%) and that the class B shallow geothermal reservoir temperature was 70.65–120.91 °C (mixed by 87.39–87.54%) in the Aba area. The class A deep geothermal reservoir temperature without cold water was 181.36–203.07 °C, and the class B deep geothermal reservoir temperature without cold water was 271.74–295.58 °C. According to the results of the δD and $\delta^{18}O$ isotope data of geothermal water analysis and calculation, the recharge elevation of the geothermal spring in the Aba area was 2876–5040 m, with an average elevation of 4473 m. The recharge area is more likely to originate from Rierlang Mountain and Xuelongbao in the north, which may be the main recharge area of the geothermal water.

Supplementary Materials: The following supporting information can be downloaded at https://www.mdpi.com/article/10.3390/su141912824/s1: Supplementary Table S1. The results of various silica and cation geothermometers. Supplementary Table S2. Relationship among temperature, enthalpy, and SiO_2 content.

Author Contributions: Conceptualization, X.Z. and Y.W.; methodology, Z.Y.; validation, Y.X.; formal analysis, X.Y. and M.S.; investigation, M.S.; resources, D.F; writing—original draft preparation, M.S. and Y.Z.; writing—review and editing, Y.Z. and X.Z.; funding acquisition, Y.W. All authors have read and agreed to the published version of the manuscript.

Funding: This paper was financially supported by the National Natural Science Foundation of China (Grant No. 42102334, 42072313), Natural Science Foundation of Sichuan Province (Grant No. 2022NSFSC0413), Opening Fund of State Key Laboratory of Geohazard Prevention and Geoenvironment Protection, Chengdu University of Technology (Grant No. SKLGP2022K017), and Fundamental Research Funds for the Central Universities (Grant No. 2682022ZTPY064).

Institutional Review Board Statement: Not applicable.

Informed Consent Statement: Not applicable.

Data Availability Statement: Not applicable.

Conflicts of Interest: The authors declare no conflict of interest.

References

1. Muther, T.; Syed, F.I.; Lancaster, A.T.; Salsabila, F.D.; Dahaghi, A.K.; Negahban, S. Geothermal 4.0: AI-enabled geothermal reservoir development-current status, potentials, limitations, and ways forward. *Geothermics* **2022**, *100*, 102348. [CrossRef]
2. Zhang, X.; Hu, Q. Development of Geothermal Resources in China: A Review. *J. Earth Sci.* **2018**, *29*, 452–467. [CrossRef]
3. Tomac, I.; Sauter, M. A review on challenges in the assessment of geomechanical rock performance for deep geothermal reservoir development. *Renew. Sustain. Energy Rev.* **2018**, *82*, 3972–3980. [CrossRef]
4. Wang, Y.; Gu, H.; Li, D.; Lyu, M.; Lu, L.; Zuo, Y.; Song, R. Hydrochemical characteristics and genesis analysis of geothermal fluid in the Zhaxikang geothermal field in Cuona County, southern Tibet. *Environ. Earth Sci.* **2021**, *80*, 1–19. [CrossRef]
5. Cheng, Y.; Pang, Z.; Kong, Y.; Chen, X.; Wang, G. Imaging the heat source of the Kangding high-temperature geothermal system on the Xianshuihe fault by magnetotelluric survey. *Geothermics* **2022**, *102*, 102386. [CrossRef]

6. Wang, Y.; Pang, Z. Heat flux measurements and thermal potential of the Garze geothermal area in the eastern Himalayan Syntaxis. *J. Volcanol. Geotherm. Res.* **2021**, *420*, 107407. [CrossRef]
7. Ai, Y.; Zhang, J.; Dong, M.; Wang, B.; Fang, G. Heat generation effects from shear friction along Xianshui river strike-slip fault in western Sichuan, China. *Geothermics* **2021**, *89*, 101936. [CrossRef]
8. Li, X.; Huang, X.; Liao, X.; Zhang, Y. Hydrogeochemical Characteristics and Conceptual Model of the Geothermal Waters in the Xianshuihe Fault Zone, Southwestern China. *Int. J. Environ. Res. Public Health* **2020**, *17*, 500. [CrossRef]
9. Liu, W.; Guan, L.; Liu, Y.; Xie, X.; Zhang, M.; Chen, B.; Xu, S.; Sano, Y. Fluid geochemistry and geothermal anomaly along the Yushu-Ganzi-Xianshuihe fault system, eastern Tibetan Plateau: Implications for regional seismic activity. *J. Hydrol.* **2022**, *607*, 127554. [CrossRef]
10. Tang, X.; Zhang, J.; Pang, Z.; Hu, S.; Tian, J.; Bao, S. The eastern Tibetan Plateau geothermal belt, western China: Geology, geophysics, genesis, and hydrothermal system. *Tectonophysics* **2017**, *717*, 433–448. [CrossRef]
11. Shi, Z.; Liao, F.; Wang, G.; Xu, Q.; Mu, W.; Sun, X. Hydrogeochemical Characteristics and Evolution of Hot Springs in Eastern Tibetan Plateau Geothermal Belt, Western China: Insight from Multivariate Statistical Analysis. *Geofluids* **2017**, *2017*, 1–11. [CrossRef]
12. Li, J.; Sagoe, G.; Yang, G.; Liu, D.; Li, Y. The application of geochemistry to bicarbonate thermal springs with high reservoir temperature: A case study of the Batang geothermal field, western Sichuan Province, China. *J. Volcanol. Geotherm. Res.* **2019**, *371*, 20–31. [CrossRef]
13. Li, B.; Shi, Z.; Wang, G.; Liu, C. Earthquake-related hydrochemical changes in thermal springs in the Xianshuihe Fault zone, Western China. *J. Hydrol.* **2019**, *579*, 124175. [CrossRef]
14. Yan, Y.; Zhou, X.; Liao, L.; Tian, J.; Li, Y.; Shi, Z.; Liu, F.; Ouyang, S. Hydrogeochemical Characteristic of Geothermal Water and Precursory Anomalies along the Xianshuihe Fault Zone, Southwestern China. *Water* **2022**, *14*, 550. [CrossRef]
15. Li, Y.; Pang, Z.; Galeczka, I.M. Quantitative assessment of calcite scaling of a high temperature geothermal well in the Kangding geothermal field of Eastern Himalayan Syntax. *Geothermics* **2020**, *87*, 101844. [CrossRef]
16. Luo, J.; Pang, Z.; Kong, Y.; Wang, Y. Geothermal potential evaluation and development prioritization based on geochemistry of geothermal waters from Kangding area, western Sichuan, China. *Environ. Earth Sci.* **2017**, *76*, 343. [CrossRef]
17. Yang, Z.; Shen, C.; Ratschbacher, L.; Enkelmann, E.; Jonckheere, R.; Wauschkuhn, B.; Dong, Y. Sichuan Basin and beyond: Eastward foreland growth of the Tibetan Plateau from an integration of Late Cretaceous-Cenozoic fission track and (U-Th)/He ages of the eastern Tibetan Plateau, Qinling, and Daba Shan. *J. Geophys. Res. Solid Earth* **2017**, *122*, 4712–4740. [CrossRef]
18. Zhang, Y.H.; Wang, Y.S.; Wang, W.S.; Liu, J.; Yuan, L.L. Zircon U-Pb-Hf isotopes and mineral chemistry of Early Cretaceous granodiorite in the Lunggar iron deposit in central Lhasa, Tibet Y, China. *J. Cent. South Univ.* **2019**, *26*, 3457–3469. [CrossRef]
19. Zhang, Y.-H.; Yao, R.-W.; Wang, Y.; Duo, J.; Cao, H.-W. Zircon U–Pb and sericite Ar–Ar geochronology, geochemistry and S–Pb–Hf isotopes of the Zebuxia Pb–Zn deposit, Tibet, southwestern China. *Ore Geol. Rev.* **2022**, *148*, 104999. [CrossRef]
20. Xinyu, Z.; Jinbao, L.; Bin, G.; Zengwu, W.; Yuting, L. Temporal and spatial characteristics of snow cover in Aba, Sichuan from 2000 to 2015. *J. Arid. Land Resour. Environ.* **2019**, *33*, 131–136. [CrossRef]
21. Wang, E.; Meng, K.; Su, Z.; Meng, Q.; Chu, J.J.; Chen, Z.; Wang, G.; Shi, X.; Liang, X. Block rotation: Tectonic response of the Sichuan basin to the southeastward growth of the Tibetan Plateau along the Xianshuihe-Xiaojiang fault. *Tectonics* **2014**, *33*, 686–718. [CrossRef]
22. Shen, B.; Wu, J.; Zhan, S.; Jin, M.; Saparov, A.; Abuduwaili, J. Spatial variations and controls on the hydrochemistry of surface waters across the Ili-Balkhash Basin, arid Central Asia. *J. Hydrol.* **2021**, *600*, 126565. [CrossRef]
23. Xiao, Y.; Hao, Q.; Zhang, Y.; Zhu, Y.; Yin, S.; Qin, L.; Li, X. Investigating sources, driving forces and potential health risks of nitrate and fluoride in groundwater of a typical alluvial fan plain. *Sci. Total Environ.* **2022**, *802*, 149909. [CrossRef] [PubMed]
24. Xiao, J.; Wang, L.; Chai, N.; Liu, T.; Jin, Z.; Rinklebe, J. Groundwater hydrochemistry, source identification and pollution assessment in intensive industrial areas, eastern Chinese loess plateau. *Environ. Pollut.* **2021**, *278*, 116930. [CrossRef]
25. Xiong, G.-Y.; Chen, G.-Q.; Xu, X.-Y.; Liu, W.-Q.; Fu, T.-F.; Khokiattiwong, S.; Kornkanitnan, N.; Seddique, A.A.; Shi, X.-F.; Liu, S.-F.; et al. A comparative study on hydrochemical evolution and quality of groundwater in coastal areas of Thailand and Bangladesh. *J. Southeast Asian Earth Sci.* **2020**, *195*, 104336. [CrossRef]
26. Kaasalainen, H.; Stefánsson, A. The chemistry of trace elements in surface geothermal waters and steam, Iceland. *Chem. Geol.* **2012**, *330–331*, 60–85. [CrossRef]
27. Alçiçek, H.; Bülbül, A.; Alçiçek, M.C. Hydrogeochemistry of the thermal waters from the Yenice Geothermal Field (Denizli Basin, Southwestern Anatolia, Turkey). *J. Volcanol. Geotherm. Res.* **2016**, *309*, 118–138. [CrossRef]
28. Chang, X.-W.; Xu, M.; Jiang, L.-W.; Li, X.; Zhang, Y.-H. Hydrogeochemical Characteristics and Formation of Low-Temperature Geothermal Waters in Mangbang-Longling Area of Western Yunnan, China. *J. Chem.* **2021**, *2021*, 1–13. [CrossRef]
29. Hou, Y.; Shi, Z.; Mu, W. Fluid Geochemistry of Fault Zone Hydrothermal System in the Yidun-Litang Area, Eastern Tibetan Plateau Geothermal Belt. *Geofluids* **2018**, *2018*, 1–13. [CrossRef]
30. Wang, X.; Wang, G.; Lu, C.; Gan, H.; Liu, Z. Evolution of deep parent fluids of geothermal fields in the Nimu–Nagchu geothermal belt, Tibet, China. *Geothermics* **2018**, *71*, 118–131. [CrossRef]
31. Marandi, A.; Shand, P. Groundwater chemistry and the Gibbs Diagram. *Appl. Geochem.* **2018**, *97*, 209–212. [CrossRef]

32. Yao, R.; Yan, Y.; Wei, C.; Luo, M.; Xiao, Y.; Zhang, Y. Hydrochemical Characteristics and Groundwater Quality Assessment Using an Integrated Approach of the PCA, SOM, and Fuzzy c-Means Clustering: A Case Study in the Northern Sichuan Basin. *Front. Environ. Sci.* **2022**, *10*, 907872. [CrossRef]
33. Xiao, Y.; Xiao, D.; Hao, Q.; Liu, K.; Wang, R.; Huang, X.; Liao, X.; Zhang, Y. Accessible Phreatic Groundwater Resources in the Central Shijiazhuang of North China Plain: Perspective From the Hydrogeochemical Constraints. *Front. Environ. Sci.* **2021**, *9*, 747097. [CrossRef]
34. Qian, J.; Peng, Y.; Zhao, W.; Ma, L.; He, X.; Lu, Y. Hydrochemical processes and evolution of karst groundwater in the northeastern Huaibei Plain, China. *Hydrogeol. J.* **2018**, *26*, 1721–1729. [CrossRef]
35. Zhang, Y.; Xu, M.; Li, X.; Qi, J.; Zhang, Q.; Guo, J.; Yu, L.; Zhao, R. Hydrochemical Characteristics and Multivariate Statistical Analysis of Natural Water System: A Case Study in Kangding County, Southwestern China. *Water* **2018**, *10*, 80. [CrossRef]
36. Zhang, Y.; Dai, Y.; Wang, Y.; Huang, X.; Xiao, Y.; Pei, Q. Hydrochemistry, quality and potential health risk appraisal of nitrate enriched groundwater in the Nanchong area, southwestern China. *Sci. Total Environ.* **2021**, *784*, 147186. [CrossRef]
37. Zhang, Y.; He, Z.; Tian, H.; Huang, X.; Zhang, Z.; Liu, Y.; Xiao, Y.; Li, R. Hydrochemistry appraisal, quality assessment and health risk evaluation of shallow groundwater in the Mianyang area of Sichuan Basin, southwestern China. *Environ. Earth Sci.* **2021**, *80*, 576. [CrossRef]
38. Xiao, Y.; Liu, K.; Yan, H.; Zhou, B.; Huang, X.; Hao, Q.; Zhang, Y.; Zhang, Y.; Liao, X.; Yin, S. Hydrogeochemical constraints on groundwater resource sustainable development in the arid Golmud alluvial fan plain on Tibetan plateau. *Environ. Earth Sci.* **2021**, *80*, 750. [CrossRef]
39. Singh, C.K.; Kumar, A.; Shashtri, S.; Kumar, A.; Kumar, P.; Mallick, J. Multivariate statistical analysis and geochemical modeling for geochemical assessment of groundwater of Delhi, India. *J. Geochem. Explor.* **2017**, *175*, 59–71. [CrossRef]
40. Liu, P.; Hoth, N.; Drebenstedt, C.; Sun, Y.; Xu, Z. Hydro-geochemical paths of multi-layer groundwater system in coal mining regions—Using multivariate statistics and geochemical modeling approaches. *Sci. Total Environ.* **2017**, *601–602*, 1–14. [CrossRef]
41. Li, X.; Huang, X.; Zhang, Y. Spatio-temporal analysis of groundwater chemistry, quality and potential human health risks in the Pinggu basin of North China Plain: Evidence from high-resolution monitoring dataset of 2015–2017. *Sci. Total Environ.* **2021**, *800*, 149568. [CrossRef] [PubMed]
42. Yang, J.; Ye, M.; Tang, Z.; Jiao, T.; Song, X.; Pei, Y.; Liu, H. Using cluster analysis for understanding spatial and temporal patterns and controlling factors of groundwater geochemistry in a regional aquifer. *J. Hydrol.* **2020**, *583*, 124594. [CrossRef]
43. Reed, M.; Spycher, N. Calculation of pH and mineral equilibria in hydrothermal waters with application to geothermometry and studies of boiling and dilution. *Geochim. Cosmochim. Acta* **1983**, *48*, 1479–1492. [CrossRef]
44. Sasaki, K.; Morita, J.; Iwaki, C.; Ueda, A. Geochemical evaluation of geothermal resources in Toyama Prefecture, Japan, based on the chemical and isotopic characteristics of hot spring waters. *Geothermics* **2021**, *93*, 102071. [CrossRef]
45. Giggenbach, W.F. Geothermal solute equilibria. Derivation of Na-K-Mg-Ca geoindicators. *Geochim. Cosmochim. Acta* **1988**, *52*, 2749–2765. [CrossRef]
46. Zhang, W.; Wang, G.; Xing, L.; Li, T.; Zhao, J. Geochemical response of deep geothermal processes in the Litang region, Western Sichuan. *Energy Explor. Exploit.* **2019**, *37*, 626–645. [CrossRef]
47. Wang, X.; Zhou, X.; Zheng, Y.; Song, C.; Long, M.; Chen, T.; Ren, Z.; Yang, M.; Li, X.; Guo, J. Hydrochemical characteristics and mixing behavior of thermal springs along the Bijiang River in the Lanping basin of China. *Environ. Earth Sci.* **2017**, *76*, 487. [CrossRef]
48. Ba, J.; Su, C.; Li, Y.; Tu, S. Characteristics of heat flow and geothermal fields in Ruidian, Western Yunnan Province, China. *Int. J. Heat Technol.* **2018**, *36*, 1203–1211. [CrossRef]
49. Yuan, J.; Xu, F.; Deng, G.; Tang, Y. Using stable isotopes and major ions to identify hydrogeochemical characteristics of karst groundwater in Xide country, Sichuan Province. *Carbonates Evaporites* **2017**, *33*, 223–234. [CrossRef]
50. Craig, H. Isotopic Variations in Meteoric Waters. *Science* **1961**, *133*, 1702–1703. [CrossRef]
51. Kong, Y.; Wang, K.; Li, J.; Pang, Z. Stable Isotopes of Precipitation in China: A Consideration of Moisture Sources. *Water* **2019**, *11*, 1239. [CrossRef]
52. Ta, M.; Zhou, X.; Guo, J.; Wang, Y.; Wang, X.; Xu, Y. Hydrogeochemical characteristics and formation of the hot springs occurring in the plunging ends of an anticline in Chongqing, Eastern Sichuan Basin, China. *Environ. Earth Sci.* **2019**, *78*, 1–14. [CrossRef]
53. Yu, J.; Zhang, H.; Yu, F.; Liu, D. Oxygen and hydrogen isotopic compositions of meteoric waters in the eastern part of Xizang. *Chin. J. Geochem.* **1984**, *3*, 93–101. [CrossRef]
54. Artemieva, I.M.; Thybo, H.; Jakobsen, K.; Sørensen, N.K.; Nielsen, L.S.K. Heat production in granitic rocks: Global analysis based on a new data compilation GRANITE2017. *Earth-Sci. Rev.* **2017**, *172*, 1–26. [CrossRef]
55. Fournier, R. Chemical geothermometers and mixing models for geothermal systems. *Geothermics* **1977**, *5*, 41–50. [CrossRef]
56. Fournier, R. Application of water geochemistry to geothermal exploration and reservoir engineering. In *Geothermal Systems: Principles and Case Histories*; Rybach, L., Muffler, L.J.P., Eds.; Wiley: Chichester, UK, 1981; pp. 109–143.